Simultaneous dual-wavelength reflection digital holography applied to the study of the porous coal samples

Alexander Khmaladze,[1,*] Alejandro Restrepo-Martínez,[2] Myung Kim,[1]
Roman Castañeda,[3] and Astrid Blandón[4]

[1]Department of Physics, University of South Florida, Tampa, Florida 33620, USA

[2]Computer Science School, Facultad de Minas, Universidad Nacional de Colombia, Sede Medellin, AA 3840, Medellin, Colombia

[3]Physics School, Facultad de Ciencias, Universidad Nacional de Colombia, Sede Medellin, AA. 3840, Medellin, Colombia

[4]Material Science School, Universidad Nacional de Colombia, Sede Medellín, AA 3840, Medellin, Colombia

*Corresponding author: akhmalad@mail.usf.edu

We present a simultaneous dual-wavelength phase-imaging digital holographic technique demonstrated on porous coal samples. The use of two wavelengths enables us to increase the axial range at which the unambiguous phase imaging can be performed, but also increases the noise. We employ a noise reduction "fine map" algorithm, which uses the two-wavelength phase map as a guide to correct a single-wavelength phase image. Then, the resulting noise of a fine map is reduced to the level of single-wavelength noise. A comparison to software unwrapping is also presented. A simple way of correcting a curvature mismatch between the reference and the object beams is offered. © 2008 Optical Society of America

OCIS codes: 180.0180, 090.1995, 090.1760, 180.6900.

1. Introduction

In conventional holography, the superposition of the wave scattered from the object and the reference wave results in an interference pattern, which is recorded on a photographic plate. Then, the hologram is developed through photochemical processes [1]. The illumination of the hologram with the reference wave results in diffraction and propagation of light in such a way that two images of the original optical field are reproduced, which retain the information of not just amplitude, but also the phase of the original optical field. One of them is the orthoscopic (i.e., exact) replica of the (object) field, while the other is its pseudoscopic (i.e., phase inverted) version.

The conventional process of holographic recording on photographic plates is rather complicated and time consuming, which makes real-time imaging difficult. In the past decade, the emphasis has been shifting to digital holography [2]. In this case, the hologram is recorded by a high-resolution CCD array [3–5]. As in the case of the ordinary holography, the hologram contains the information not just of the amplitude distribution of light, but also of its phase. After the hologram recording, the extraction of the amplitude and phase can be accomplished by numerically propagating the reference wave. The complete and accurate description of the propagation of the optical field by diffraction theory allows numerical reconstruction of an image as an array of complex numbers, which represent the amplitude and the phase of the optical field [6]. In addition to the ability of fast image acquisition and the retrieval of both quantitative amplitude and phase information, digital holography offers the versatility of various image processing techniques that can be applied to the complex field, which may not be feasible in real space holography. A number of

different methods have been considered for numerical reconstruction including Fresnel transform, Huygens convolution, and angular spectrum [7–9].

Application of digital holography in microscopy is especially important, because of the extremely narrow depth of focus of high-magnification systems [10,11]. Microscopic imaging by digital holography has been applied to image microstructures and biological systems [12–14]. Numerical focusing of holographic images can be accomplished from a single exposed hologram. Direct accessibility to the phase information can be used for numerical correction of different aberrations of the optical system, such as field curvature and anamorphism [15]. Phase-contrast techniques convert the phase changes suffered by the light wave, while passing through or reflecting from objects, into observable intensity variations. Over the years, a number of techniques have been developed to qualitatively perform this conversion. The examples include Zernike phase-contrast (ZPC) microscopy and differential interference contrast (DIC) microscopy. In ZPC microscopy, a phase plate and spatial filtering converts the phase into intensity modulation. DIC microscopy, also known as Nomarski interference contrast (NIC), uses interferometry of two polarized light beams that take slightly different paths through the sample. The length of the optical paths differ from each other and the beams interfere when they are recombined, which gives the appearance of three-dimensional imaging.

ZPC and DIC phase-contrast microscopy techniques cannot be easily used to quantify the phase change since the conversion of phase to intensity modulation is nonlinear. Since the phase change indicates the change in the optical path length, it can then be converted to physical thickness, providing the sample's height information. Thus, the direct access to the quantitative phase information makes digital holographic microscopy (DHM) a true three-dimensional (3D) imaging technique.

However, the phase imaging of objects whose optical thickness variation is greater than the wavelength of light becomes ambiguous and gives rise to phase wrapping. When the total phase change exceeds 2π, the phase wraps and the image suffers a discontinuity. We have previously introduced a dual-wavelength phase-imaging technique that removes the 2π discontinuities by generating two phase images (called phase maps) using two different wavelengths [16]. The usual software algorithmic approaches to phase unwrapping often are computationally intensive and cannot handle certain complex phase topologies. This method, on the other hand, removes the discontinuities by simply comparing the two phase maps. It then reduces the phase noise by comparing the resulting dual-wavelength phase map to one of the original single-wavelength phase maps. The dual-wavelength method allows imaging to be performed faster, with the only time constriction being the speed at which the two Fourier transforms for both wavelengths are performed. In the case of a complicated phase topology, such as porous material, the software unwrapping algorithm can mistakenly identify low intensity areas as multiple phase steps, producing nonexisting height features. On the other hand, in dual-wavelength phase imaging, all the observed height features are real.

Activated coals, as well as coals treated with pyrolysis, are highly porous materials. This is the reason these coals have a high capacity for absorption, which makes them very important in processes such as purification and filtering. These processes often depend on the size and morphology of the pores. Normally, porosity is evaluated using chemical methods, but these techniques can be rather complex and time consuming. Optical microscopy and digital imaging analysis have been used previously [17] to investigate coal samples, but these methods have their own limitations in terms of the minimum pore size that can be observed. As it was mentioned earlier, ordinary microscopic techniques do not provide the 3D depth information about the sample. The porosity evaluation using atomic force microscopy (AFM) fails as the pores are too deep for the tip. Such limitations in analyzing the pores of coal samples can be overcome by reflection DHM as shown in this work.

2. Experimental Setup

Figure 1 shows the experimental setup, based on two overlapping Michelson interferometers that enable us to fine-tune the location of the first-order components associated with each wavelength in the Fourier space. Its configuration is similar to the setups based on the modified Mach–Zehnder [18–22] and on the Michelson interferometers [23–25], as typical for
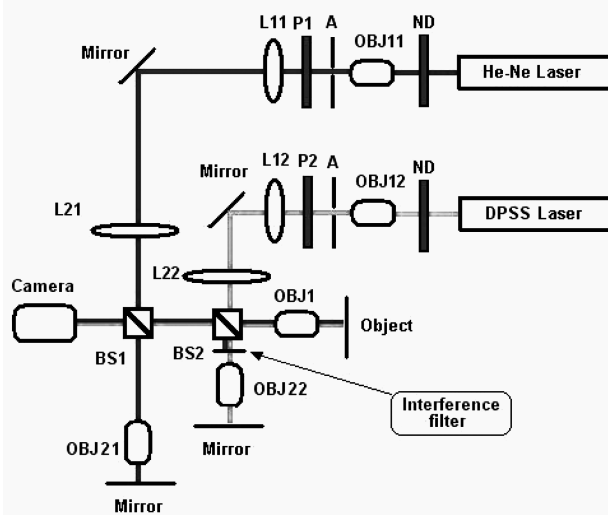

Fig. 1. Multiwavelength digital holography setup. The lateral magnification of all microscope objectives (OBJ) is 20×. The focal lengths of lenses L21 and L22 are 17.5 cm and 10 cm, respectively. The ND filters and polarizers P1 and P2 are used to control the intensity of the laser beams. Pinholes A are used to select only the central part of the Gaussian beam. Lenses L11, L12, L21, and L22 and objectives OBJ1, OBJ21, and OBJ22 ensure an appropriate collimation of the waves (i.e., the beam waist is kept at "infinity").

reflection DHM. He–Ne ($\lambda_1 = 633\,\text{nm}$) and diode-pumped solid-state ($\lambda_2 = 532\,\text{nm}$) lasers were used as light sources. Neutral density filters (ND) control the intensity of the laser beams. 20× microscope objectives OBJ11 and OBJ12, together with pinholes A and the collimator lenses L11/L12, produce uniform plane waves, whose intensity is further controlled by polarizing filters P1 and P2. Beam splitters BS1 and BS2 divide the beams into the reference and the object waves, which are reflected by the reference mirrors and the object. Thereafter, the beam splitters direct the waves toward the CCD camera.

Lenses L21 and L22 and 20× microscope objectives OBJ21 and OBJ22 again collimate the reference waves. Two separate reference arms are used to match the object path lengths for each object wave. The interference filter, introduced into the reference arm of the diode-pumped solid-state laser, allows only this wavelength to pass and blocks the other laser. The 20× microscope objective OBJ1 focuses a magnified image of the sample onto the sensor of the CCD camera, where the interference pattern between the reflected reference and object waves is recorded.

An angle between the object wave and each of the reference waves can be introduced by slightly tilting the reference mirrors. Furthermore, by tilting the two reference beams orthogonally to each other, we can precisely control the location of each spectral component in Fourier space [Fig. 2(c)]. As a result, the two spectral components can be sufficiently separated to enable the effective filtering in the Fourier domain, which in turn allows for the real-time imaging.

3. Multiwavelength Phase-Imaging Digital Holography

A. Angular Spectrum Method with the Curvature Correction

The angular spectrum algorithm is used for reconstructing the phase and the amplitude information of the optical field from the recorded hologram. It has a number of advantages over the more commonly used Fresnel transform or Huygens convolution methods. The angular spectrum $A_0(k_x, k_y; 0)$ of an arbitrary field with intensity distribution $E_0(x, y; z = 0)$ can be obtained using the Fourier transform

$$A_0(k_x, k_y; 0) = \iint E_0(x, y; 0) \exp[-i(k_x x + k_y y)]\mathrm{d}x\mathrm{d}y,$$

(1)

where k_x and k_y are spatial frequencies corresponding to x and y, respectively. In the case of digital holography, $E_0(x, y; z = 0)$ is the intensity distribution recorded by the CCD camera, which constitutes the digital hologram, and Eq. (1) is numerically evaluated. So, the angular spectrum $A_0(k_x, k_y; 0)$ consists of a zero order and a pair of first-order components, the latter corresponding to the twin holographic images.

Figure 2(a) displays the image plane digital hologram of a United States Air Force (USAF) resolution target, recorded using the experimental setup in Fig. 1. The target, which originally was a clear piece of glass with a chromium pattern on it, was uniformly covered with a 100 nm layer of aluminum to make it entirely reflective. As a result, the pattern became almost invisible to a naked eye, but the features were elevated by 100 nm with respect to the background. The interference patterns of the hologram, due to the two wavelengths, can be seen in Fig. 2(b), and Fig. 2(c) shows the Fourier spectrum of the hologram, in which the two pairs of first-order components, corresponding to the two wavelengths, are clearly visible.

The angular spectrum can then be propagated in space along the z axis as follows:

$$A(k_x, k_y; z) = A_0(k_x, k_y; 0) \exp[ik_z z],$$

(2)

where $\exp[ik_z z]$ is the complex transfer function of the propagation, with $k_z = \sqrt{k^2 - k_x^2 - k_y^2}$, where $k = 2\pi/\lambda$. At this stage, the Fourier-domain filtering can be applied to block the unwanted spectral terms and to select each of the first-order components. It can be performed with a numerical band-pass filter if the off-axis angle of the reference beam is properly adjusted. Finally, a complex wave field is reconstructed by simply performing the inverse Fourier transform, i.e., numerically evaluating the integral:

$$E(x, y; z) = \iint A(k_x, k_y; z) \exp[i(k_x x + k_y y)]\mathrm{d}k_x\mathrm{d}k_y.$$

(3)

A significant computational advantage of the angular spectrum method is that once the angular spectrum at $z = 0$ is known, only one additional Fourier transform should be applied for reconstructing the object wave at any plane z. Furthermore, there is no requirement for z to be larger than a certain minimum value, as in the case of the Fresnel integral.

In spite of the collimating configuration of the experimental setup (Fig. 1), some wavefront curvature remains in each wave. Moreover, because these curvatures are not equal, a curvature mismatch appears
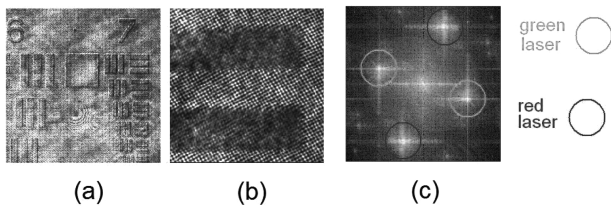

Fig. 2. Two-wavelength DHM of a USAF resolution target: (a) digital hologram, (b) small section of the hologram in (a) showing two fringe patterns due to the recording wavelengths (the rectangular shadows are two bars of the target image) and (c) Fourier spectrum of the hologram in (a); the encircled sections are the first-order components for the red and the green wavelengths, respectively.

in the final phase image as shown in Fig. 3(a). To understand this, consider the complex field captured by a CCD matrix [see Fig. 3(c)]. The phase mismatch can be compensated for numerically, by multiplying the original "flat" field $E_0(x, y; z = 0)$ by the phase factor $\exp[i\phi]$, where $\phi = kd$ is the phase difference between points a and o and d is the optical path difference. From geometry, $(R + d)^2 = R^2 + r^2$, or $R + d = \pm\sqrt{R^2 + r^2}$, which after discarding the negative solution leads to $d = \sqrt{R^2 + r^2} - R$. Now, to put this all together:

$$E(x, y; 0) = E_0(x, y; 0) \exp\left[ik\left(\pm\left[\sqrt{R^2 + r^2} - R\right]\right)\right], \quad (4)$$

which is the exact expression for the curvature corrected field. The value of R can be experimentally determined for a given setup. The sign in Eq. (4) depends on whether the image of the flat area is convex or concave. By adjusting this sign and the magnitude of R in the optical setup, the residual mismatch in the optical wavefront curvature is properly compensated [Fig. 3(b)].

B. Phase and Height Maps

The object surface is described by height map $h(x, y)$, which is determined from phase map $\phi(x, y)$ of the holographic reconstruction at a given wavelength by

$$h(x, y) = \frac{\lambda}{4\pi}\phi(x, y). \quad (5)$$

Figure 4(a) shows the phase map of the aluminum-covered USAF resolution target. The step size
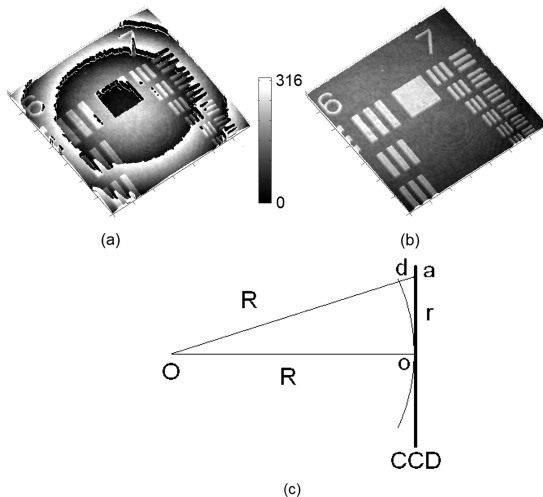

Fig. 3. Reconstructed phase image of the USAF resolution target (a) without curvature correction and (b) with curvature correction (the vertical scale is in nanometers); (c) the diagram illustrating the curvature correction procedure. R is the wave's radius of curvature, which can be determined experimentally for a given setup. $r = \sqrt{x^2 + y^2}$ is the distance between the center of the CCD matrix (point o) and an arbitrary point a. x and y are the coordinates of a.
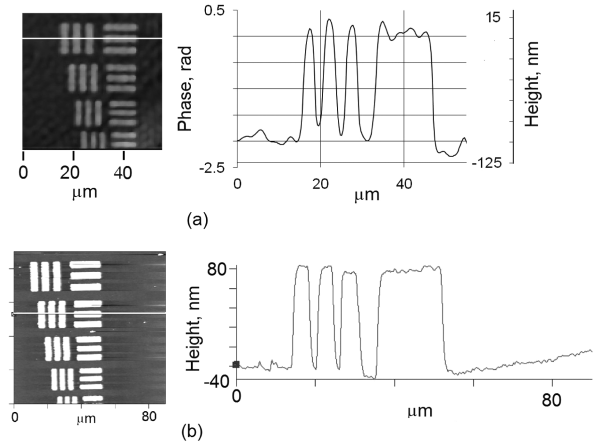

Fig. 4. (a) Phase map and height profile for $\lambda = 633\,\text{nm}$. The profile is taken along the line over the phase map. (b) AFM image and height profile that confirm the results in (a).

is approximately 2.2 rad. According to Eq. (5), it is proportional to the target height map, whose profile corresponding to the line over the phase map in Fig. 4(a) is sketched. The step height is about 100 nm. This result is confirmed by the AFM scan shown in Fig. 4(b).

C. Multiwavelength Phase Imaging

As stated before, the phase images of objects with variations in optical thickness greater than the wavelength are ambiguous and result in phase wrapping. Consequently, the phase map exhibits discontinuities at the positions where the total phase change exceeds 2π. However, if the simultaneous dual-wavelength phase imaging is performed, the discontinuities of the two maps will occur at different positions, since the two wavelengths are different. It allows unwrapping the phase by comparing the two maps, as stated below. In this way, the 2π jumps are removed and then the phase ambiguities are resolved.

Figure 5 shows the phase images of the USAF resolution target imaged at an angle. The images produced with single wavelengths exhibit multiple phase steps [Fig. 5(a) and 5(b)]. Phase maps ϕ_1 and ϕ_2, derived from each wavelength are subtracted, so that $\phi_{12} = \phi_1 - \phi_2$ is obtained. Adding 2π wherever $\phi_{12} < 0$ yields a new phase map, practically free of discontinuities. It is equivalent to a phase map created by a single synthetic "beat" wavelength

$$\Lambda_{12} = \lambda_1 \lambda_2 / \left|\lambda_1 - \lambda_2\right|. \quad (6)$$

For wavelengths $\lambda_1 = 633\,\text{nm}$ and $\lambda_2 = 532\,\text{nm}$, the beat wavelength is $\Lambda_{12} = 3334\,\text{nm}$ [Figs. 5(c) and 5(d)]. Notice that while the phase images produced by a single wavelength exhibit multiple discontinuities, in the final synthetic wavelength map the discontinuities are removed. In fact, here the synthetic wavelength is such that the range of the dual-wavelength phase map is barely enough to resolve the discontinuities [some even remain on the left and right of Fig. 5(c)].
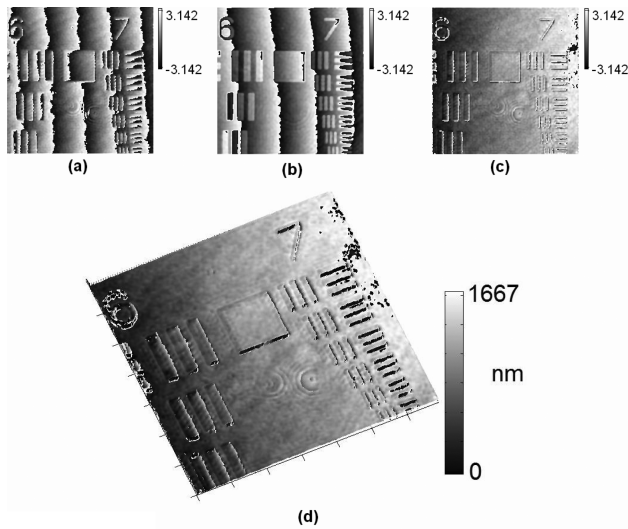
Fig. 5. Phase maps for (a) $\lambda_1 = 532$ nm and (b) $\lambda_2 = 633$ nm. (c) Synthetic dual-phase map with beat wavelength $\Lambda_{12} = 3334$ nm and (d) its 3D rendering (the images are $174 \times 174 \,\mu\text{m}^2$ and the vertical scale for (a)–(c) is in radians).

D. Application of the Phase Noise Reduction Algorithm

The drawback of the dual-wavelength method is the amplification of phase noise by the same factor as the range. Furthermore, the two phase maps differ in their noise distributions, so that the final dual-wavelength phase map can remain quite noisy even if the noise in the single-wavelength phase maps is low. However, one can use this dual-wavelength "coarse" map as a guide, together with one of the original phase maps (ϕ_1 or ϕ_2), to produce the low noise "fine" phase map. The method (detailed in Ref. [16]) involves dividing the height of the coarse map into the integer number of one of the original wavelengths, say λ_1. Then, the wavelength high segments from phase map ϕ_1 are pasted into this coarse map, which achieves the desired effect of reduced noise together with extended range. In practice, the areas near the boundaries of the wavelength intervals are somewhat problematic. There, the noise present in single-wavelength map ϕ_1 causes the height to change erratically by one wavelength. In order to partially solve this problem, one can compare this map to the coarse map and, if the difference is more than $\lambda_1/2$, add or subtract λ_1 depending on the size of the difference. However, if the noise is excessive, the last step results in the shift of small portions of the final image by λ_1 from its true position. Since the height of such a shift is always λ_1, it can be partially fixed by software by looking for the steps of this height and shifting them up (or down) by λ_1.

Indeed, the high noise level makes it very difficult to measure the height of the object's individual features from the dual-wavelength phase map, as shown by the height profile in Fig. 6(a) obtained from the map in Fig. 5(c), despite the fact that the overall shape of the object is still preserved by the dual-phase map. In contrast, the height profile of the fine
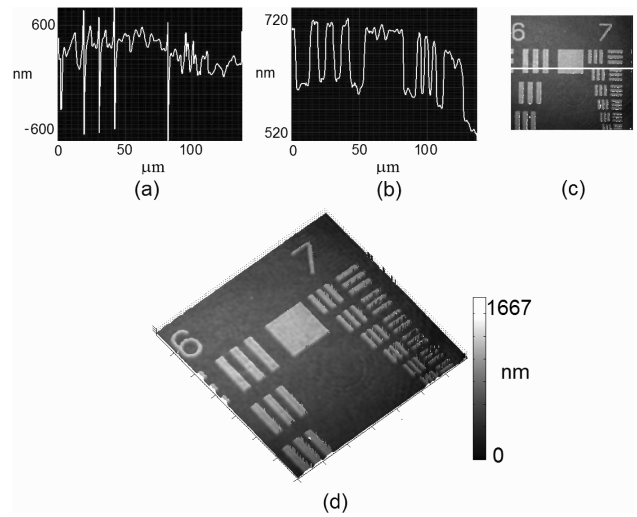

Fig. 6. Height profiles of (a) coarse and (b) fine phase maps. (c) Final fine map and (d) 3D rendering of (c). The image sizes are $174 \times 174 \,\mu\text{m}^2$.

map, shown in Fig. 6(b), again yields the step height of 100 nm.

To numerically estimate the noise levels in the system, the height profiles of the flat area for a single wavelength, a coarse map, and a fine map (Fig. 7) were taken and their rms noise was measured. While the rms noise in the coarse map is substantial (on the order of 54 nm), the noise for the fine map is almost equal to the single-wavelength phase map (on the order of 8.5 nm and 6.5 nm, respectively).

4. Imaging of Porous Coal Samples

The technique outlined here has been successfully applied to the 3D imaging of coal samples. The samples were acquired from the Coal Group at the National University of Colombia, Campus Medellin. These samples were treated by pyrolysis and prepared in a mixture with epoxy resin; then they were ground and polished with aluminum oxide abrasives (1, 0.5, and 0.03 μm grain size). The process ensured that the samples are reflective and firm enough to be imaged.
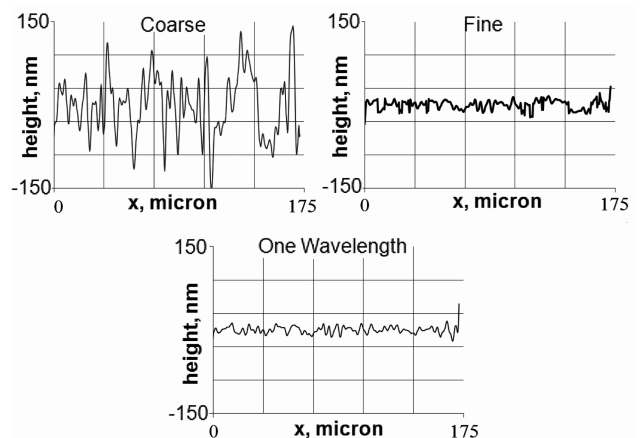

Fig. 7. Line intensity profiles of a flat area for the coarse, fine, and the single-wavelength phase maps, respectively.

A. Two-Wavelength Optical Phase Unwrapping

In Fig. 8, a boundary between the porous coal and the resin is shown. The amplitude image [Fig. 8(a)] is similar to what a regular microscope would display. The area corresponding to the resin is at the lower right corner. It is apparent that the boundary is barely visible in the amplitude image, as there is no significant difference between the reflection from the coal and resin.

Figures 8(b) and 8(c) show the single-wavelength phase images, which display multiple discontinuities
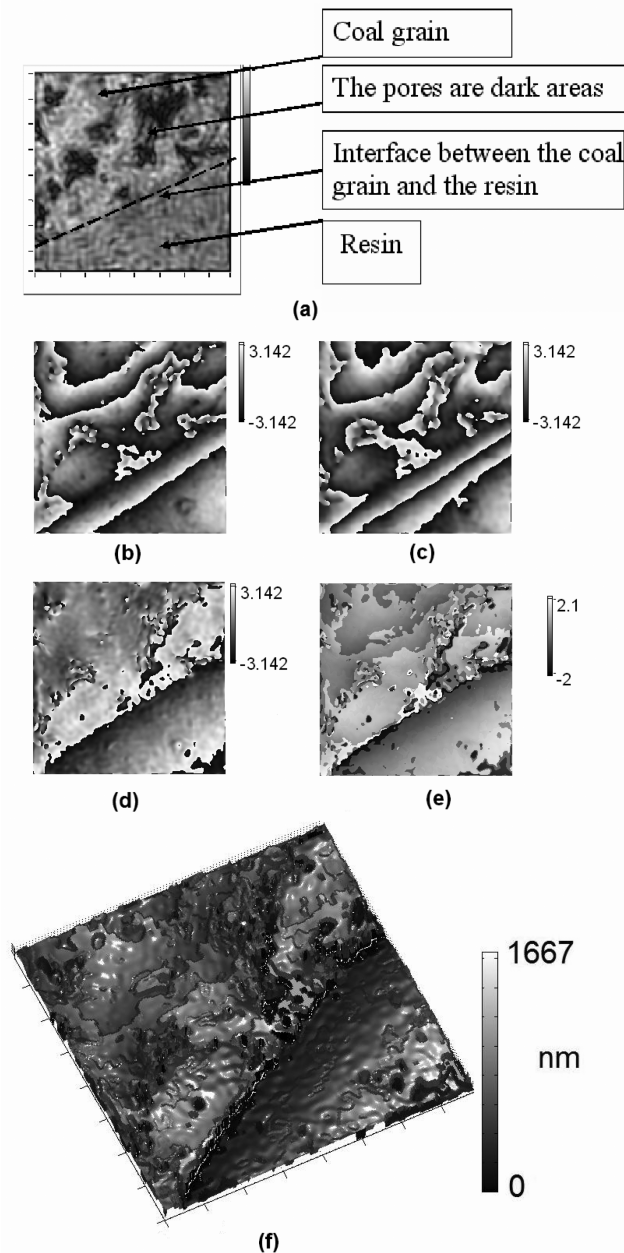

(a)

(b)   **(c)**

(d)   **(e)**

(f)

Fig. 8. Images of a porous coal sample: (a) amplitude image; phase maps reconstructed at (b) $\lambda_1 = 0.63\,\mu$m and (c) $\lambda_2 = 0.53\,\mu$m; (d) the dual-wavelength coarse phase map, (e) fine map, and (f) its 3D rendering. All images are $98 \times 98\,\mu$m^2 and vertical scale (b–e) is in radians.

that were removed in the dual-wavelength coarse map [Fig. 8(d)]. The phase noise is significantly reduced in the fine map [Fig. 8(e)], as appreciated in its 3D rendering [Fig. 8(f)]. The latter image shows the 3D surface profiles of the coal and the resin surfaces, which appear to "bend" towards each other at the boundary between the two surfaces, so the boundary itself is seen very clearly.

B. Comparison between Dual-Wavelength and Software Phase Unwrapping

Figure 9 shows the images of porous coal samples treated with pyrolysis. Once again, the phase images at a single wavelength clearly exhibit 2π phase steps [Figs. 9(b) and 9(c)], while the dual-wavelength unwrapped phase map in Fig. 9(d) shows very few discontinuities. The parts of the images where discontinuity is still present correspond to low reflectivity areas on the sample hologram, where no interference pattern is visible. Consequently, the phase there is basically random noise, which gives rise to multiple 2π phase jumps. These can generally be identified as deeper pores. With this method, pores with a lateral size on the order of a micrometer can be identified.
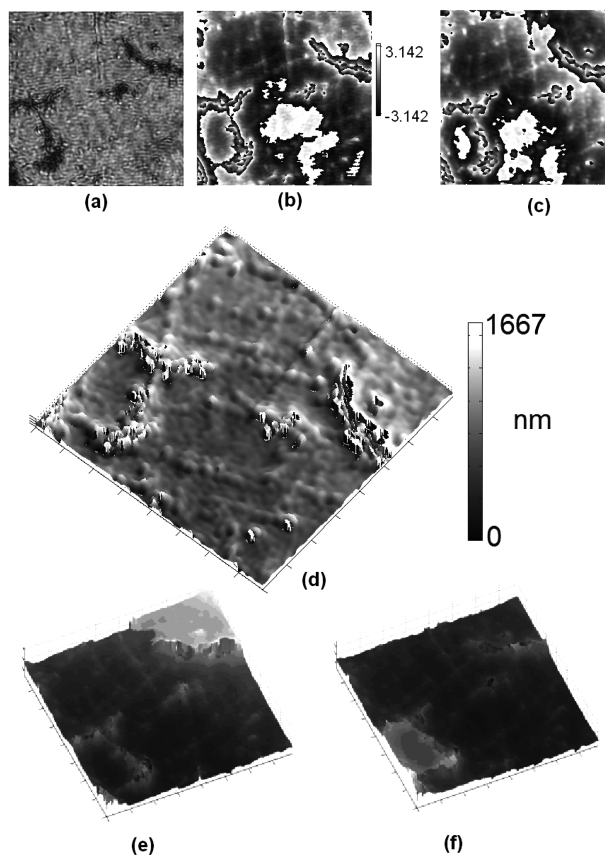

(a)   **(b)**   **(c)**

(d)

(e)   **(f)**

Fig. 9. Images of a porous coal sample: (a) amplitude image; phase maps reconstructed at (b) $\lambda_1 = 532\,$nm and (c) $\lambda_2 = 633\,$nm; (d) 3D rendering of the dual-wavelength phase map; software unwrapped phase maps reconstructed at (e) $\lambda_1 = 633\,$nm and (f) $\lambda_2 = 532\,$nm for comparison. All image sizes are $98 \times 98\,\mu$m^2. The vertical scales of the phase maps are in radians.

It is worth noticing that unwrapping the single-wavelength phase images using conventional algorithms is very problematic, as illustrated in Figs. 9(e) and 9(f). A typical software unwrapping algorithm starts at a certain point of an image and moves along a one-dimensional (1D) path (e.g., straight line, spiral). If it encounters what looks like a phase wrap, it shifts the map down or up. If the image has noisy areas [corners in Figs. 9(e) and 9(f)] where phase oscillates randomly, the software algorithm takes it as a real feature and creates nonexistent steps in phase/height profile, which clearly do not correspond to the real height profile of the sample.

C. Application of the Fine Map Algorithm

Figure 10 shows the images of an activated porous coal in a resin sample. The areas on the left and right sides of the image are too dark, but the central region is well illuminated. Two vertical scratches due to the coal-polishing process are clearly visible. Figures 10(a) and 10(b) represent the coarse and the fine phase maps, respectively. A noise reduction by a factor of 5 is apparent by comparing the height profiles in Fig. 10(c) and 10(d) from the coarse and the fine maps, respectively. For further comparison, the single-wavelength phase map and the same line profile are sketched in Figs. 10(e) and 10(f), respectively.

The "spots" in the images Fig. 10(c) and 10(d), as well as the spike around $120\,\mu m$ in Fig. 10(f), result from the high level noise in the single-wavelength images. Consequently, some of the wavelength segments are erroneously shifted by a wavelength (see Subsection 3.D). Artifacts like these are rare and they do not prevent us from obtaining an accurate 3D picture of the sample. From the depth information available from the fine map [Fig. 10(d)], one can see, for example, that the depth of a small feature (scratch located around $75\,\mu m$ from the left on all the line profiles) is about 100 nm, which is again consistent with the single-wavelength phase map [Fig. 10(f)]. Obviously, the single wavelength possesses multiple artifacts due to phase wrapping.

5. Conclusion

The dual-wavelength phase-imaging digital holography technique proved to be a powerful method of 3D imaging with the 2π ambiguity resolved. Its application to the detection and study of pores in coal samples has been demonstrated. The method is advantageous in comparison to the software unwrapping approaches as it requires no intensive computation procedures and can handle complex phase topologies. The method provides high-resolution, accurate quantitative profiles of surfaces and can be an effective tool in studying small and large scale 3D features of many natural and man-made samples. The use of two wavelengths together with the fine map algorithm allows us to increase the maximum height of the features that can be imaged, while keeping the noise low (few nanometers). The same method can also easily be applied to imaging in transmission rather than reflection, which can be extremely useful for imaging of biological samples and obtaining the density profiles of cells. The simultaneous dual-wavelength setup utilized together with the angular spectrum algorithm provides an easy way to acquire single frame images in real-time, which can be used to study cell migration, for instance.

The selection of two wavelengths that are closer to each other increases the axial range, but also increases the noise to the levels where the fine map algorithm begins to fail. To further increase the axial range and still keep the final noise levels low, the same procedure can be applied at three or more wavelengths. Furthermore, it is possible to use a tunable laser to iteratively increase the range while reducing the noise to the desired levels [2]. The proposed method of curvature correction is simple enough to easily implement the same experiment without the microscope objectives in the reference arms of the Michelson interferometer. This would greatly simplify the optical setup and make the initial adjustments of the interferometers much easier.
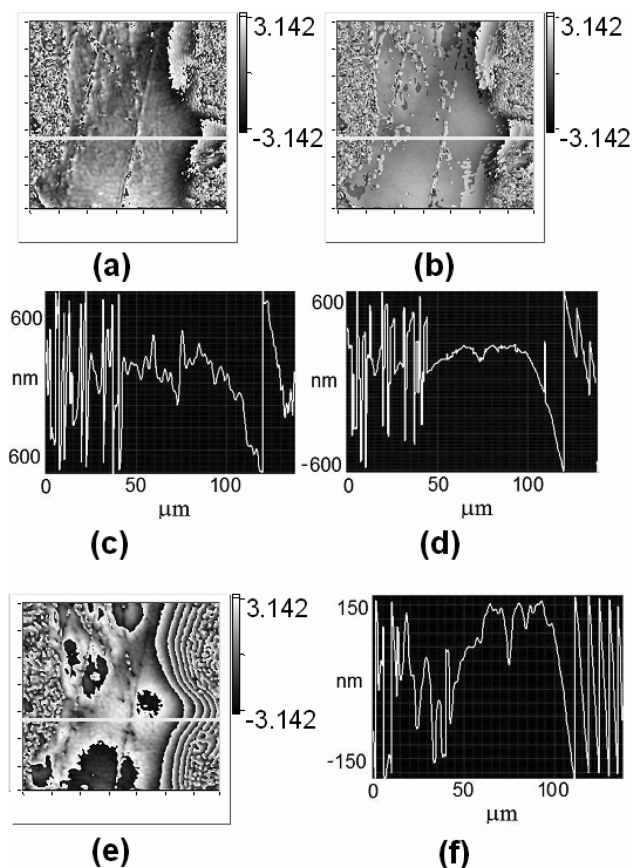
Fig. 10.   (a) Coarse phase map, (b) fine phase map, and line profiles for (c) coarse and (d) fine. For comparison, (e) single-wavelength phase map at $\lambda = 633$ nm and (f) line profile (the image sizes are $138 \times 138\,\mu m^2$ and the vertical scales of the phase images are in radians).

References

1. P. Hariharan, *Optical Holography*, 2nd ed. (Cambridge University, 2004).
2. W. Jueptner and U. Schnars, *Digital Holography*, (Springer Verlag, 2004).
3. U. Schnars, "Direct phase determination in hologram interferometry with use of digitally recorded holograms," J. Opt. Soc. Am. A **11**, 2011–2015 (1994).
4. U. Schnars and W. P. Jueptner, "Direct recording of holograms by a CCD target and numerical reconstruction," Appl. Opt. **33**, 179–181 (1994).
5. U. Schnars and W. P. O. Jueptner, "Digital recording and numerical reconstruction of holograms," Meas. Sci. Technol. **13**, R85–R101 (2002).
6. J. W. Goodman, *Introduction to Fourier Optics*, 2nd ed. (McGraw-Hill, 1996).
7. S. Grilli, P. Ferraro, S. De Nicola, A. Finizio, G. Pierattini, and R. Meucci, "Whole optical wavefields reconstruction by digital holography," Opt. Express **9**, 294–302 (2001).
8. L. F. Yu and L. L. Cai, "Iterative algorithm with a constraint condition for numerical reconstruction of a three-dimensional object from its hologram," J. Opt. Soc. Am. A **18**, 1033–1045 (2001).
9. K. Matsushima, H. Schimmel, and F. Wyrowski, "Fast calculation method for optical diffraction on tilted planes by use of the angular spectrum of plane waves," J. Opt. Soc. Am. A **20**, 1755–1762 (2003).
10. A. Barty, K. A. Nugent, D. Paganin, and A. Roberts, "Quantitative optical phase microscopy," Opt. Lett. **23**, 817–819 (1998).
11. E. Cuche, F. Bevilacqua, and C. Depeursinge, "Digital holography for quantitative phase-contrast imaging," Opt. Lett. **24**, 291–293 (1999).
12. L. Xu, X. Peng, J. Miao, and A K. Asundi, "Studies of digital microscopic holography with applications to microstructure testing," Appl. Opt. **40**, 5046–5051 (2001).
13. W. S. Haddad, D. Cullen, J. C. Solem, J. W. Longworth, A. McPherson, K. Boyer, and C. K. Rhodes, "Fourier-transform holographic microscope," Appl. Opt. **31**, 4973–4978 (1992).
14. W. Xu, M. H. Jericho, I. A. Meinertzhagen, and H. J. Kreuzer, "Digital in-line holography for biological applications," Proc. Natl. Acad. Sci. (U.S.) **98**, 11301–11305 (2001).
15. P. Ferraro, S. De Nicola, A. Finizio, G. Coppola, S. Grilli, C. Magro, and G. Pierattini, "Compensation of the inherent wave front curvature in digital holographic coherent microscopy for quantitative phase-contrast imaging," Appl. Opt. **42**, 1938–1946 (2003).
16. J. Gass, A. Dakoff, and M. K. Kim, "Phase imaging without 2π-ambiguity by multiple-wavelength digital holography," Opt. Lett. **28**, 1141–1143 (2003).
17. W. Branch and H. J. Mesa, "Caracterización de poros de carbones tratados térmicamente empleando procesamiento digital de imágenes y microscopía asistida por computador," Adv. Comput. Syst. **1**, 35–39 (2004).
18. K. Tobin and P. Bingham, "Optical spatial heterodyned interferometry for applications in semiconductor inspection and metrology," Proc. SPIE **6162** (2005).
19. J. Kühn, T. Colomb, F. Montfort, F. Charrière, Y. Emery, E. Cuche, P. Marquet, and C. Depeursinge, "Real-time dual-wavelength digital holographic microscopy with a single hologram acquisition," Opt. Express **15**, 7231–7242 (2007).
20. P. Ferraro, L. Miccio, S. Grilli, M. Paturzo, S. De Nicola, A. Finizio, R. Osellame, and P. Laporta, "Quantitative phase microscopy of microstructures with extended measurement range and correction of chromatic aberrations by multiwavelength digital holography," Opt. Express **15**, 14591–14600 (2007).
21. D. Parshall and M. K. Kim, "Digital holographic microscopy with dual wavelength phase unwrapping," Appl. Opt. **45**, 451–459 (2006).
22. M. K. Kim, L. Yu, and C. J. Mann, "Digital holography and multi-wavelength interference techniques," in *Digital Holography and Three-Dimensional Display*, T. C. Poon, ed. (Springer, 2006), Chap. 2.
23. N. Warnasooriya and M. K. Kim, "LED-based multi-wavelength phase imaging interference microscopy," Opt. Express **15**, 9239–9247 (2007).
24. A. Khmaladze and M. Kim, "Quantitative phase contrast imaging of cells by multi-wavelength digital holography," in *Conference on Lasers and Electro-Optics (CLEO)*, Technical Digest (CD), (Optical Society of America, 2007), paper JTuA52A.
25. A. Khmaladze, C. J. Mann, and M. K. Kim, "Phase contrast movies of cell migration by multi-wavelength digital holography," in *Digital Holography and Three-Dimensional Imaging (DH)*, Technical Digest (CD), (Optical Society of America, 2007), paper DMB3.